Polarimetric WSR-88D network, observation highlights

Dusan Zrnic[1], Robert Lee[2], and Jami B. Boettcher[3]

[1]*NOAA/National Severe Storms Laboratory, Norman OK, USA*

[2]*NOAA/Radar Operation Center, Norman OK, USA*

[3]*NOAA/Weather Decision Training Branch, Norman OK, USA*

1. Introduction

The dual polarization upgrade of the U.S. Doppler weather radar (WSR-88D) network was completed in spring of 2013. During and after the deployment process, legacy radar data and the new polarimetric fields were carefully monitored by a data quality team comprised of personnel from the Radar Operation Center (ROC), the Weather Decision Training Branch (WDTB), and the National Severe Storms Laboratory (NSSL). Throughout this monitoring process interesting observations predicated by meteorological conditions specific to radar sites have been made. Furthermore, for some time during and following the deployment, the WDTB provided "Storm of the Month" nationwide seminars on the internet to exchange experiences among the National Weather Service (NWS) forecasters. Herein are shown examples of polarimetric variables from a few operational radars and in different weather conditions as well as non-weather events.

2. Meteorological Phenomena

Radar polarimetry has emerged as a leading contender for solving remotely the rain measurement problem. The United States may benefit from using polarimetry compared to conventional Doppler radar. Over a period of 20 years, flood damage may be reduced by about $ 2.7 billion (referenced to year 2003, Zrnic 2003). Better management of water resources is estimated to add another $ 115.2 billion of savings in the same twenty year span. Benefits such as better warnings, separation of meteorological from non-meteorological returns, and classification of non-meteorological scatterers, are less quantifiable, but have greatly improved forecaster's understanding of a spectrum of hazardous weather events. Here we present potent features such as tornado debris signatures, hail, three body scattering, and transition from snow to rain.

2.1 Tornado debris signature

The debris lofted by a tornado is seen as a prominent decrease in the correlation coefficient, $\rho_{hv,}$ between the horizontally and vertically polarized returns and a local minimum of about 0 dB in differential reflectivity, Z_{DR}. This feature has become popular forecasters' evidence of tornado touchdown. Violent tornadoes lift debris to great heights as seen in Fig 1. This tornado was an

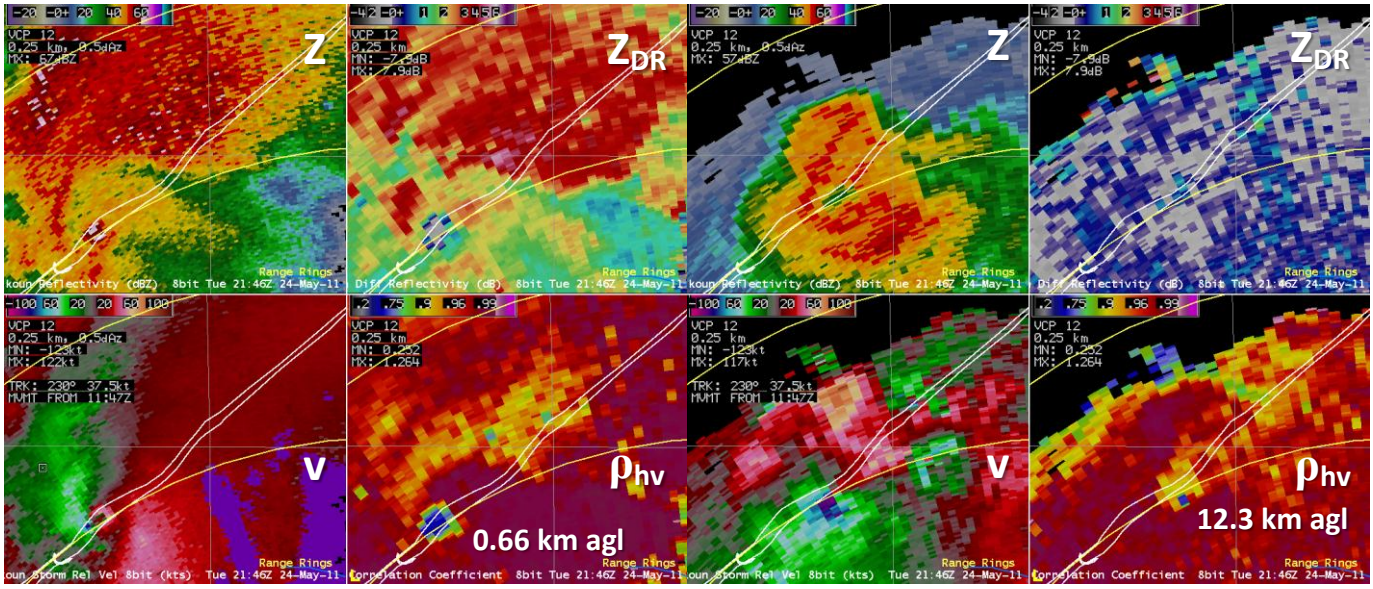

a) b)

Fig. 1. a) Fields of reflectivity, differential reflectivity, storm relative velocity and correlation coefficient from a tornadic storm of May 24, 2011, time 2146 UTC. The elevation is 0.5^o and the height of beam center at the debris location is 0.66 km above ground level. The velocity scale on the color bar is in knots. The damage path is superimposed. b) Same as in a) except the elevation is 10^o. The first range ring is at 60 km from the radar the second at 80 km.

EF-5 and occurred on May 24, 2011 near Oklahoma City. It had a path length of over 100 km, caused nine fatalities and more than 100 injuries.

The localized minima of ρ_{hv} at both elevations (Fig. 1a, b) are lower than 0.7 km, are well defined, and coincide with the damage path on the ground. At the lowest elevation the Z_{DR} is close to zero. But at higher elevations it cannot be easily discerned from its background negative values, possibly because vertically aligned crystals are present or a slight calibration offset is not accounted for. Note that the tornado vortex signature seen in the velocity field is collocated with the localized minimum in the correlation coefficient field. It is significant that the debris was lofted more than 12 km above ground (Fig. 1b). Similar findings prompted meteorologists from the National Weather Service to examine many cases of TDS in an attempt to relate its characteristics to tornado intensity.

The summary finding by this investigation is depicted in Fig. 2 as a graph of maximum height of the TDS versus the Enhanced Fujita scale. Evident is the separation of the EF-3 (maximum winds larger than 217 km h^{-1}) and stronger tornados from the weaker ones.

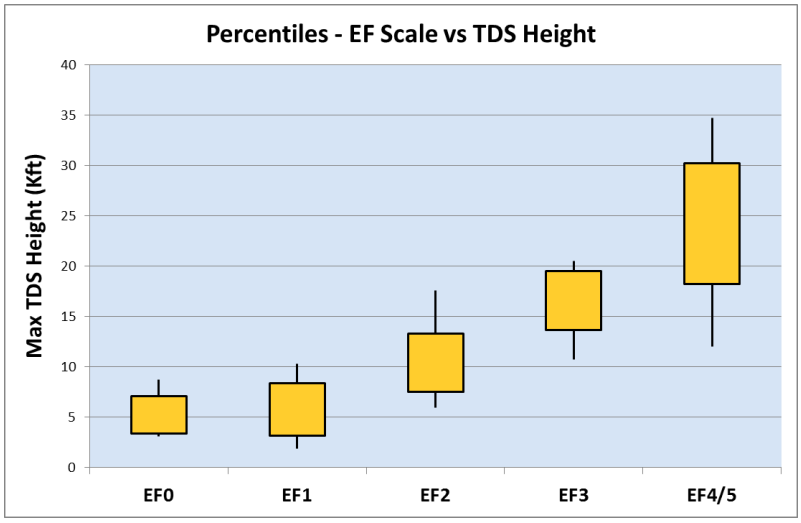

Fig. 2. Maximum height of the Tornado Debris Signature plotted against tornado intensity. The intensity is measured on the Extended Fujita scale. Figure courtesy Chad Entremont, National Weather Service.

2.2 Large hail

Much work is ongoing at NSSL in trying to devise automated ways to classify hail. Of principal interest is large hail with a diameter between 2.5 and 5 cm and giant hail with a diameter exceeding 5 cm. The operational hydrometeor classification algorithm has one category for hail and it is designated "rain hail mixture" (Park et al. 2009). In the future, the size discrimination will be done within this category. An example of classification (Fig. 3) shows that hail coincides with well pronounced low Z_{DR} (a round region of close to 0 dB values indicated by the arrow) and a depression in ρ_{hv} also indicated by the arrow. The feature of extended negative Z_{DR} west of the local Z_{DR} minimum is the three body scattering signature (Zrnic 1987. The negative values are expected as scattering of the vertically polarized waves by hail to the ground extends over large circular rings. Hence the corresponding backscatter to the hail is stronger at this polarization (Hubert and Bringi 2000). Coincident with the negative Z_{DR} are low values of correlation coefficient (blue in Fig. 3). The hydrometeor classification algorithm produces credible results over most of the field. These are rain (light green) and heavy rain (dark green) and biological scatterers (light gray, to the north-east and south-east). There are obvious misses such as biological scatterers in the region of the three body scattering signature and at the back of the storm (west end). There, the category of unknown scatterers (pink color) exonerates the algorithm to some small degree. After all, the hydrometeor classification algorithm has not been "trained" to detect three body scattering signatures.

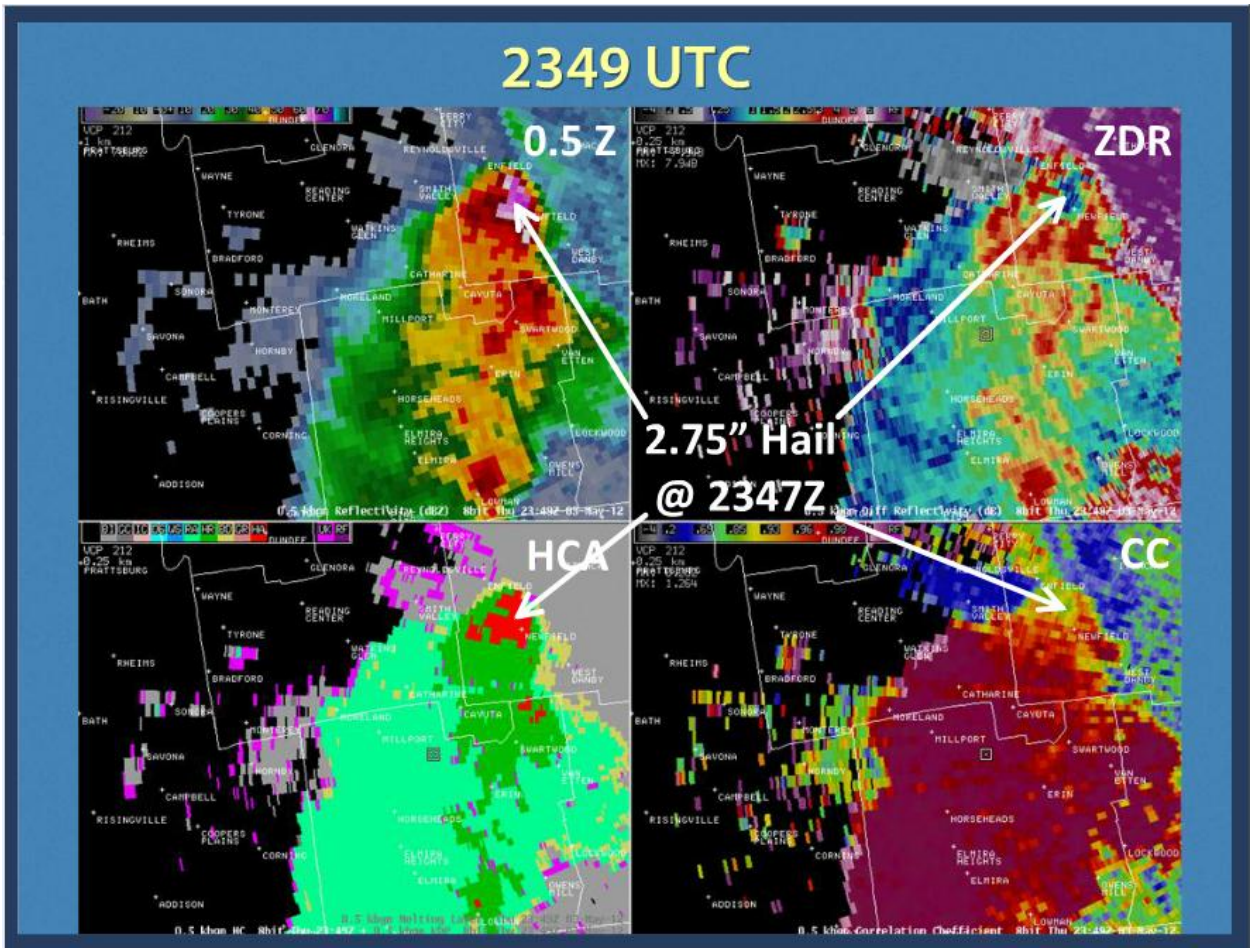

Fig. 3. Field of reflectivity, differential reflectivity, classified hydrometeors (HCA), and correlation coefficient (CC) on May 3, 2012, obtained by the radar in Albany New York. Maximum hail size is indicated in inches (about 7 cm). The radar location is to the right.

2.3 Lowering of snow level

An observation of lowering of the melting layer behind a cold front was reported by forecasters in Phoenix, Arizona. The two images (Fig. 4) illustrate this episode. It was caused by an advancing cold front. The melting layer is characterized by the lower values (0.9 to 0.95) of ρ_{hv} and noisier speckled appearance compared to the homogenous values above and below it. Lowering of the melting layer helped forecast snow at the ground in this mountainous state. Behind the front the melting layer is 0.7 km to 1 km below its value of about 2.4 km ahead of the front. This creates the oblong shape to projection of the conical scan on the flat surface as depicted in Fig. 4a. An hour later the front has pushed east and lowered the right side of the melting layer. The shape tightens up in a well-defined circle and the melting layer is at about 1.2 km above ground level. Forecasters used this information to warn the public of snow hazards on the surrounding mountain roads.

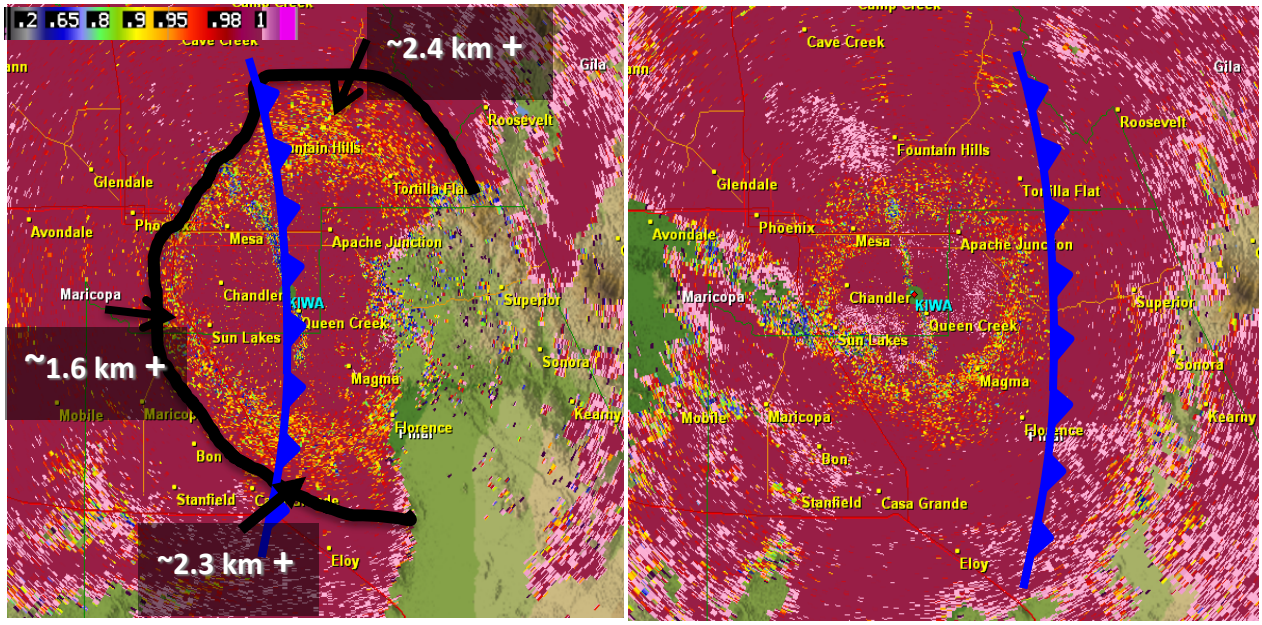

(a) (b)

Fig. 4. Fields of the correlation coefficient obtained with the radar in Phoenix Arizona on Nov 5, 2011. a) Time of observation is 7:30 UTC (0:30 local time) and the height of the melting layer above ground is indicated as well as the position of the cold front. b) Similar to a) but the time is one hour later. The melting layer has a shape of a ring and has dropped to about 1.2 km above ground. The cold front has moved beyond the melting layer ring.

2.4 Snow rain boundary

In winter months about 2/3 of the USA is exposed to snow storms. The correct location in real time of the transition from rain to snow has great value to ground transportation, public, and electric utilities. Shortly after the weather radar in Wichita, Kansas, was upgraded to dual

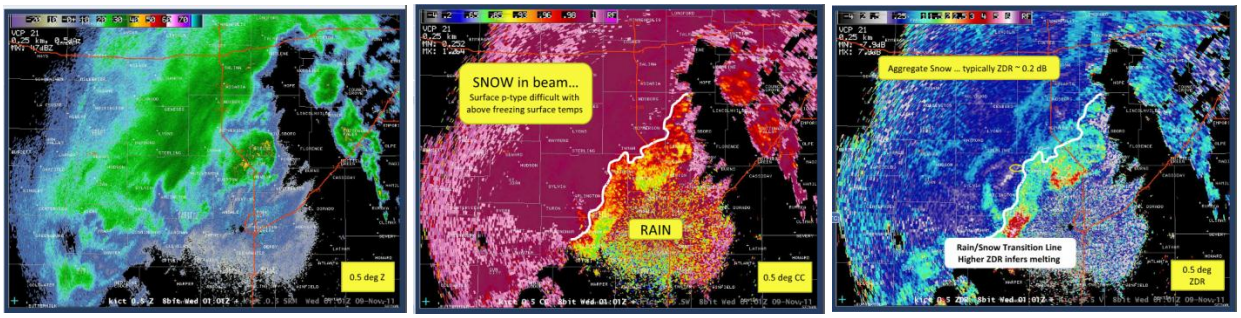

Fig. 5. Fields of Z , ρ_{hv}, and Z_{DR}. The radar is located in Wichita, Kansas, and the data were collected on 9-Nov-2011, at 20:01 local time (EST).

polarization a significant snow event occurred over its coverage area. The fields of Z, ρ_{hv}, and Z_{DR} (Fig. 5) illustrate the added value dual polarization brought to forecasters. Without in situ observations there are no clues in the Z field about the types of precipitation. The ρ_{hv} field exhibits a sharp transition between high values in dry snow (> 0.98) to the North West and lower values (< 0.95) in wet snow South East. A band of enhanced Z_{DR} (1 to 3 dB) confirms that the snow is melting.

3. Other observations

Herein we highlight observations other than precipitation or tornadoes. These include chaff, ocean, insects, birds and smoke plumes.

3.1 Chaff

Over the contiguous US, chaff is often released as part of training exercises by the military. To maximize reflections chaff needles are typically one half of the military radar wavelength long. Fig. 6 presents chaff observed by the Phoenix, Arizona radar. Reflectivity values 20 and 30 dBZ are seen and values of correlation coefficient less than 0.6 warn that these are not meteorological scatterers. The negative values of Z_{DR} are intriguing because in free fall chaff is expected to be horizontally oriented (Zrnic and Ryzhkov 2004). Observations by other WSR-8Ds also indicate occasional negative values for which we have no definitive answers. It could

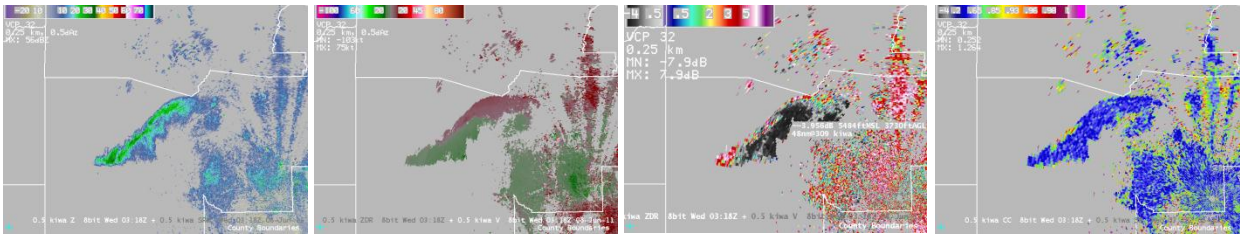

Fig. 6. Fields of Z , Doppler velocity v, Z_{DR}, and ρ_{hv}. The vertical extent of the figures is 95 km, and the data are from the Phoenix Arizona radar, on 08- June – 2011, 20:18 local time.

be that strong electric fields orient these needles vertically or that there is significant vertical shear of horizontal wind. For example assuming that Brussaard (1976) derivation can be applied to the angle β between the chaff axis and the horizontal plane we obtain $\tan(\beta) = sw/g$, where s is the shear, w terminal velocity of chaff, and g acceleration due to gravity. Assuming $s = 1$ m s^{-1} one can quickly infer that unrealistically high values of shear are needed to tilt the shaft more than 45^{o}.

3.2 Ocean, sea spray, insects, and birds

The fields in Fig. 7 are mostly over the Atlantic Ocean off the coast of North Carolina. Along the North West corner is the coast and the sea breeze boundary (rope like feature) of the Z field

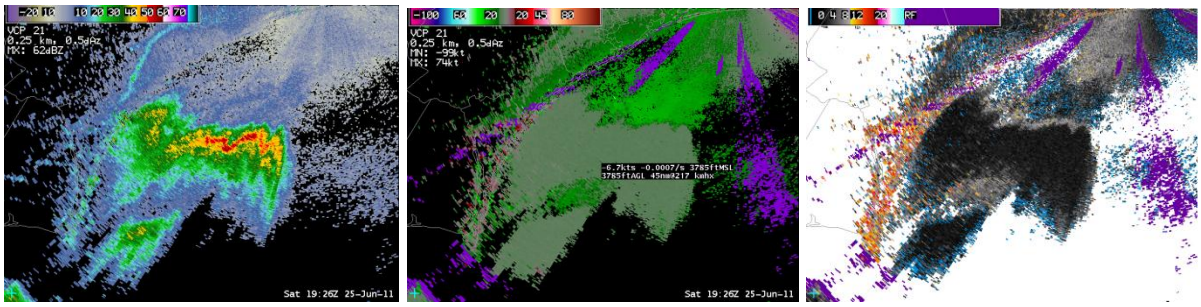

Z *v* Spectrum width

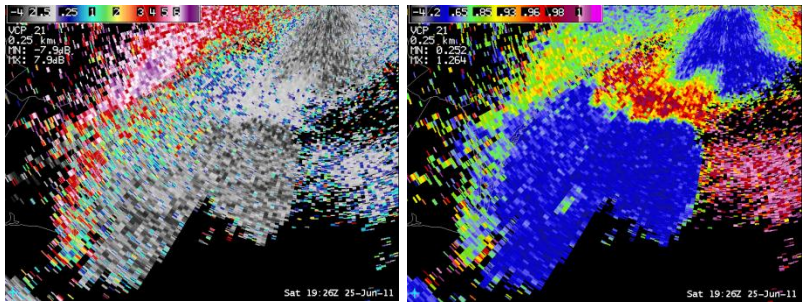

Z_{DR} ρ_{hv}

Fig. 7. Fields of *Z*, Doppler velocity *v*, spectrum width, Z_{DR}, and ρ_{hv}. The radar is in Morehead North Carolina. Date is 25-June- 2011, time 12:26 local time (MST).

is not apparent in any of the other variables. Moderately low ρ_{hv} (0.85 to 0.95) and high Z_{DR} (> 6 dB) suggests insect are present. The coast line is very well delineated by the abrupt increase in the spectrum width from about 2 m s^{-1} to over 12 m s^{-1}. We attribute this feature to coastal birds as the differential reflectivity is at most 3 dB. The increase in spectrum width is likely due to flapping of the wings and differential radial motion of birds in the resolution volume. From the speckled field of Doppler velocities in that area it can be inferred that the birds are not migrating but likely scouting in search of food.

Particularly noteworthy is the central area in these figures. The region of high *Z* and smooth low values of *v* is likely due to returns from the sea that the beam intercepted as it was bent during propagation. The Z_{DR} field in this region is quite negative as expected from sea clutter. The ρ_{hv} values less than 0.65 (blue color) are consistent with returns from the ocean. The values of about 0.95 coincide with the region where the velocities are high and toward the radar while Z_{DR} is close to 0. This could be a region where the bending beam is intercepting sea spray before hitting the ocean surface.

3.3 Smoke plumes

On June 4, 2012 a lightning-sparked fire started near Ruidoso New Mexico and it took over twenty days to contain this fire. In terms of human structures this was the most destructive fire in New Mexico history. It burned about 45000 acres and 254 buildings. The images of Z and Z_{DR} that were obtained on June 8 delineate a storm like feature (Fig. 7). The values of Z range from

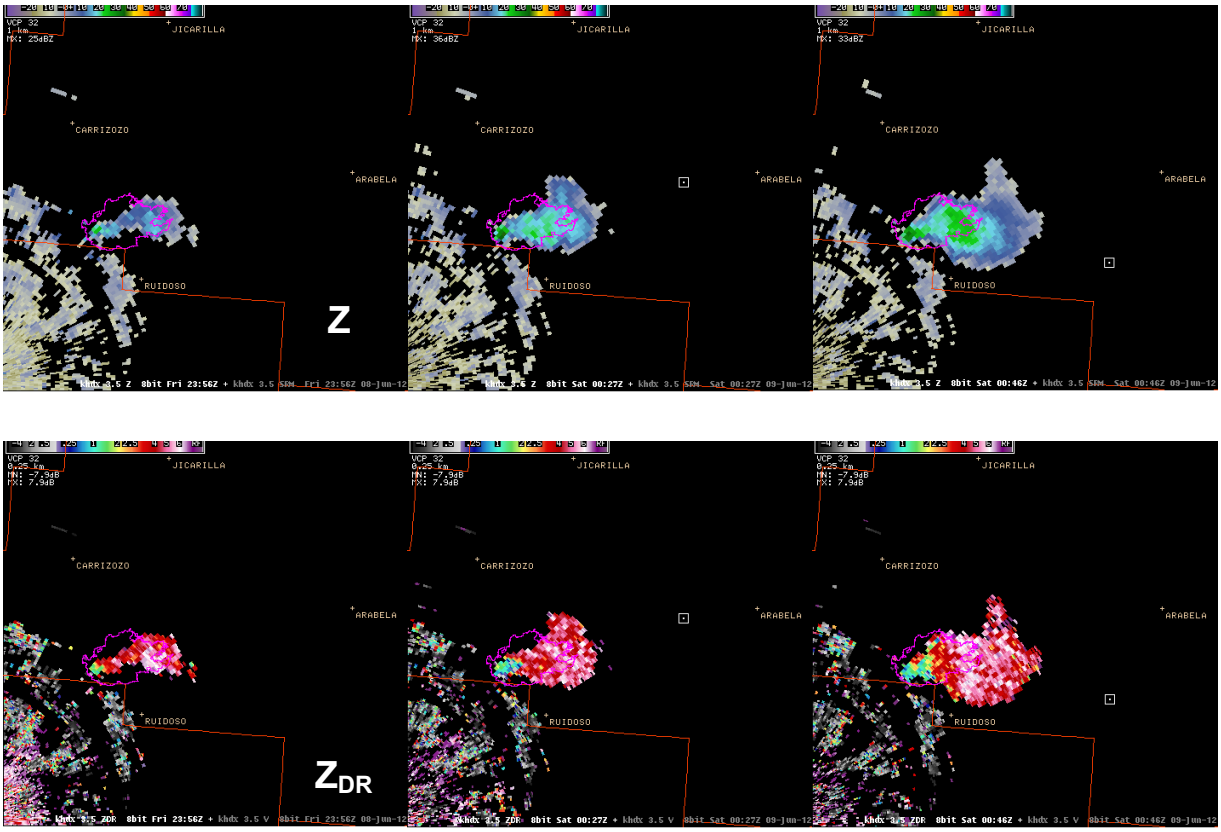

Fig. 8. Top, fields of Z at 6 pm, 6:30 pm and 6:50 pm on 8-June- 2012 observed with the radar in Holloman Air Force Base, New Mexico. The storm like feature is the large smoke plume caused by the Little Bear fire in the Ruidoso area.

0 to about 35 dBZ, with the higher values in the south-west portion of the reflectivity field. The Z_{DR} field has a local minimum smaller than 2 dB while throughout the rest of the plume the values are larger than 3 dB. The local minimum is in the updraft and caused by lofting of larger scatterers. Further downwind, these scatterers fall out leaving smaller horizontally oriented burnt debris. Locating the updraft can be very useful to fire fighters as it pin-points the origin of active fire.

4. Summary

Examples of polarimetric fields observed by the data quality team and by NWS forecasters were shown. Tornado debris signatures associated with violent tornadoes extended up to 12 km above ground; the observed maximum debris heights correlated well with the tornado intensity. Lowering of the melting layer caused by a cold front and the progressive descent of the snow level in the mountains of Arizona prompted forecasters to amend their outlook. In a snowstorm in America's heartland, a clear delineation of transition between snow and rain improved snow warnings. A smoke plume was observed to have a localized minimum of differential reflectivity above the fire initiation area in the midst of otherwise large values associated with the advecting plume. Chaff can have positive and negative differential reflectivity; some physical mechanisms that could produce such values have been suggested. Quite often several types of scatterers were identified in a scan. For example a sharp contrast in values of polarimetric variables was observed over the ocean between regions where the ocean contribution dominates and where sea spray is the main ingredient. In addition the mean velocity and spectrum width add motion information that further helps identify scattering types. These and other examples (not shown or discussed) illustrate the potency of this large polarimetric network of radars to quickly identify an intriguing spectrum of signatures associated with diverse climate regions and environments.

Acknowledgement

We are grateful to our colleagues from NWS, ROC, WDTB, and NSSL for overseeing the upgrade to dual polarization, maintaining the radars, as well as providing the data.

References

Brussaard, G., 1976: A meteorological model for rain-induced cross polarization. IEEE Trans. Antennas and Propag., **AP-24,** 5-11.

Hubbert. J.C., and V.N. Bringi, 2000: The effects of three-body scattering on differential reflectivity signatures. *J. Atmos. Oceanic technol.,* **17,** 51-61.

Ryzhkov, A.V., T.J. Schuur, D.W. Burgess, and D.S. Zrnic, 2005: Polarimetric tornado detection. *J. Appl. Meteor*. **44,** 557-570.

Park, H-S., A. V. Ryzhkov, D. S. Zrnic, and K. E. Kim, 2009: The hydrometeor classification for the polarimetric WSR-88D; description and application to an MCS. *Wea. Forecasting*, **24,** 730-748.

Zrnic, D., 2003: Cost Benefit Analysis (.doc, 44 kB), NOAA/NSSL report, 5 pp, available at http://www.nssl.noaa.gov/publications/wsr88d_reports/.

Zrnic, D.S. and A.V.Ryzhkov, 2004: Polarimetric properties of chaff. *J. Atmos. Oceanic Technol.*, **21**, 1017-1024.

Zrnic, D.S., 1987: Three-Body Scattering Produces Precipitation Signatures of Special Diagnostic Value, *Radio Sci*., **22**, 76-86.